Parabolic refractive X-ray lenses

Bruno Lengeler,* Christian G. Schroer, Boris Benner, Achim Gerhardus, Til Florian Günzler, Marion Kuhlmann, Jannik Meyer and Christiane Zimprich

II. Physikalisches Institut, RWTH Aachen, D-52056 Aachen, Germany. E-mail: lengeler@physik.rwth-aachen.de

Parabolic refractive X-ray lenses are optical components, especially suitable for third-generation synchrotron radiation sources. This article describes the status of the development of our lenses and illustrates the possibilities for micrometre and submicrometre focusing and for X-ray imaging in absorption and phase contrast. The parabolic lens profile ensures distortion-free imaging of high quality. First characteristics of Be lenses are given. A microscope based on Be lenses is expected to have a lateral resolution below 80 nm.

Keywords: parabolic refractive X-ray lenses; X-ray microscopy; X-ray microanalysis; tomography.

1. Introduction

X-ray diffraction, X-ray analysis in the micrometre and submicrometre range and imaging with X-rays have found a broad spectrum of applications in physics, chemistry, materials science and life sciences. Mirrors (Kirkpatrick & Baez, 1948; Hignette *et al.*, 2001), multilayers (Underwood *et al.*, 1986, 1988), capillaries (Bilderback *et al.*, 1994; Hoffman *et al.*, 1994), Fresnel zone plates (Lai *et al.*, 1992), Bragg–Fresnel zone plates (Aristov *et al.*, 1989; Chevallier *et al.*, 1995) and waveguides (Lagomarsino *et al.*, 1997; Feng *et al.*, 1998) are the standard optical components for generating a microfocus for hard X-rays in combination with synchrotron radiation sources. Refractive X-ray optics of various designs (Snigirev *et al.*, 1996; Elleaume, 1998; Lengeler *et al.*, 1999a,b; Kohmura *et al.*, 1999; Cederström *et al.*, 2000, 2001; Dudchik *et al.*, 2000; Piestrup *et al.*, 2000; Aristov *et al.*, 2000) which have been developed recently extend the list of these optical components. In this article we describe the characteristic features of parabolic refractive X-ray lenses (PRXLs) for microanalysis and imaging designed and fabricated at the Aachen University of Technology (Lengeler *et al.*, 1999a,b).

Glass lenses are among the oldest optical components, with an extremely broad spectrum of applications. This is due to the outstanding properties of glass concerning homogeneity, reproducibility, strong refraction and low absorption for visible light. On the other hand, for X-rays in condensed matter, refraction is weak and absorption is strong as expressed in the index of refraction, $n = 1 - \delta + i\beta$, by the small refractive decrement δ of order 10^{-6} and the large absorption coefficient $\mu = 4\pi\beta/\lambda$ when compared with the values for visible light in glass. For that reason, refractive X-ray lenses were long considered as not feasible. However, refraction of X-rays in matter is not zero and absorption is not infinite, and refractive lenses for hard X-rays with a focal length in the range of 1 m and below have been developed in the last five years.

2. Concept of parabolic refractive X-ray lenses

A number of aspects had to be taken into account for manufacturing refractive X-ray lenses. First, the radius of curvature R of the refracting surfaces must be small, in fact below 1 mm, if reasonably short focal distances are to be achieved with a small number of lenses. As a consequence, the geometrical aperture of the lens is typically 1 mm and happens to match perfectly the beam size of undulator sources in third-generation synchrotron radiation sources. Second, many lenses are stacked in a row in order to increase the refractive power. The focal length, f, in the thin-lens approximation is then given by

$$f = R/2N\delta, \tag{1}$$

where N is the number of lenses in the stack. With N between 10 and a few 100, a focal length of 1 m is feasible below about 40 keV. Third, the mass absorption coefficient, μ/ρ, decreases as Z^3/E^3 by photoabsorption and then levels off below 0.2 cm^2 g^{-1} when Compton scattering dominates μ/ρ (Lengeler *et al.*, 1999a). As a consequence, even for hard X-rays, above about $E = 5$ keV, only the lightest elements with a low atomic number Z, like Li, Be, B, C and Al, are suitable as lens material. Ni is a suitable candidate for energies around 100 keV.

A substantial improvement in the performance of refractive X-ray lenses was achieved at our institute by the development of a novel manufacturing technique by which the lenses are shaped as a double paraboloid of rotation (Fig. 1). Details are given by Lengeler *et al.* (1999a,b). Note the concave form of the lenses which is a consequence of the real part $1 - \delta$ in the index of refraction being smaller than 1. The merit of this procedure, as compared with the initial row of drilled holes (Snigirev *et al.*, 1996), is in the suppression of spherical aberration and in the focusing in both directions. This allows for achieving a focal spot size in the submicrometre range. This is also a prerequisite for imaging by means of refractive X-ray lenses. The transmission of a stack with N lenses is given by (Lengeler *et al.*, 1999a)

$$T = \left[1 - \exp(-2a_p)\right](2a_p)^{-1}\exp(-\mu Nd), \tag{2}$$

with

$$2a_p = \frac{\mu N R_0^2}{R} = \frac{\mu}{\rho}\frac{R_0^2}{f\lambda^2}C, \quad C = \frac{\pi}{N_a r_0}\frac{A}{Z + f'(E)}, \tag{3}$$
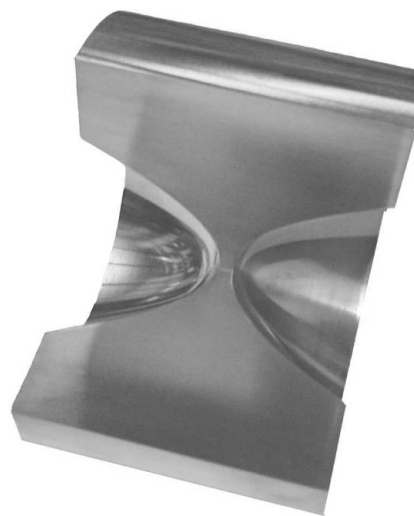
Figure 1
Model of an aluminium refractive X-ray lens with double parabolic profile. One quadrant has been removed in order to show the lens profile. In reality the geometric aperture $2R_0$ is about 1 mm in diameter.

and where d is the distance between the apices of the parabolas in a lens. N_a is Avogadro's constant, r_0 is the classical electron radius, A is the atomic mass and $Z + f'(E)$ is the atomic form factor in the forward direction. Note that for a given X-ray energy E the transmission depends only on the inverse focal length and on the mass absorption coefficient μ/ρ, which is an atomic property only dependent on the atomic number Z and independent of the density. Away from absorption edges of the lens material, C is almost constant for all elements. A focal length substantially below 30 cm will lead to a poor transmission even for low-Z elements as lens material. The form fidelity and the surface finish of the lenses are characteristics which afford special care. With modern CNC machines it is possible to generate a rotational parabolic shape within 1 µm and a surface roughness below 0.1 µm. Fig. 2 shows the cross sections through Al, Ni and Be lenses which demonstrates the high quality of our manufacturing technique concerning form fidelity and surface roughness. The profiles were measured with a white-light interferometer. At the steep flanks of the embossed parabola the amount of backscattered light becomes very weak. Therefore, only the bottom area with a diameter of about 150–200 µm is shown in Fig. 2. For aluminium lenses, this area corresponds to the effective aperture of the lens. Therefore, large figure errors would be detected and avoided prior to X-ray optical tests at the synchrotron radiation source. Small figure errors that arise during the state-of-the-art manufacturing process do not measurably affect the X-ray optical properties of the lens. For beryllium lenses, however, only the central part of the effective aperture can be investigated by white-light interferometry. For these lenses it may become necessary to quantify the overall figure error by X-ray optical imaging. This will require the systematic investigation of aberrations.

There is an important point about roughness which should be mentioned. For a high-quality X-ray mirror surface the root-mean-square roughness σ must be below a few 0.1 nm. Refractive lenses give excellent results even when the roughness is up to a few 100 nm. This much lower sensitivity to roughness of lenses compared with mirrors makes the manufacturing process of lenses much less demanding. The effect can be understood in the following way. Roughness σ enters in the transmitted intensity in both cases as a damping factor, $\exp(-2NQ^2\sigma^2)$, where $N = 1$ for a mirror and where Q is the momentum transfer. For a lens, $Q = k_1 - nk_1 = \delta k_1$ is of the order 10^{-5} Å^{-1} whereas for a mirror $Q = 2k_1\theta_1 \simeq 2 \times 10^{-2}$ Å^{-1} if the
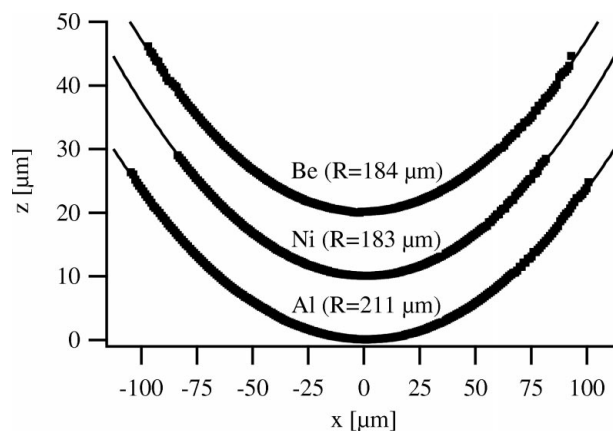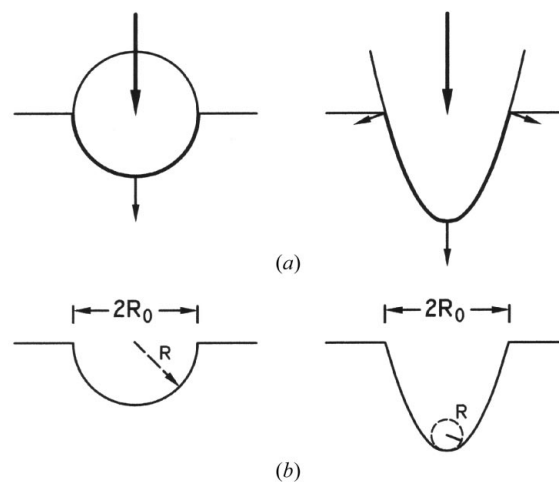
angle of total reflection θ_1 is of the order of 0.1°. The much larger momentum transfer in a total reflecting mirror must be compensated by a much lower surface roughness σ in order to generate the same damping factor as in a stack of lenses. Note that the roughnesses in the individual lenses are independent from one another, so that it is N rather than N^2 which enters in the damping factor $\exp(-2NQ^2\sigma^2)$.

We would like to insist that a parabolic lens profile has major advantages compared with a spherical profile as generated, for example, by impressing a sphere from a ball-bearing in the lens material. First, parabolic lenses are free of spherical aberration, resulting in a small spot size and in almost distortion-free imaging, as demonstrated below. Secondly, parabolic profiles can be generated with higher accuracy as explained in Fig. 3. A parabolic tool always generates a force component normal to the surface reducing the tendency for microcracks and hence for profile errors and surface roughness. In contrast, a sphere generates at the equator line only shear forces without compression. Thirdly, as shown in Fig. 3, the radius of curvature R and the geometrical aperture $2R_0$ are decoupled from one another for a parabola whereas they are not for a sphere. For parabolic lenses it is possible to combine a geometrical aperture of 1 mm with a radius of curvature R of 200 µm and below. The smaller the value of R, the lower is the focal length f and the smaller is the number of lenses needed in a stack.

3. Applications of parabolic refractive X-ray lenses

We will now discuss two main fields of application for parabolic refractive X-ray lenses: first, the generation of a micrometre and submicrometre focus for diffraction, fluorescence, absorption and reflectometry; second, magnified imaging in absorption and phase contrast and tomography.

The generation of an X-ray microfocus is based on the demagnification of an X-ray source on the sample. The smaller the source size the smaller will be its image. Therefore, a low-β undulator will generate a smaller focus than a high-β undulator at the expense of flux in the microbeam, since the beam divergence is larger for the low-β undulator, reducing the beam intensity at the aperture of the lens. The demagnification $m = L_2/L_1 = f/(L_1 - f)$ can be a factor of 100 or more. There is no need for an order-sorting aperture as in

Figure 2
Height profiles of an aluminium, a nickel and a beryllium lens measured by white-light interferometry. The profiles are displaced in the vertical by 10 µm. The parabolic fit gives the quoted values of R and a surface roughness far below 1 µm.
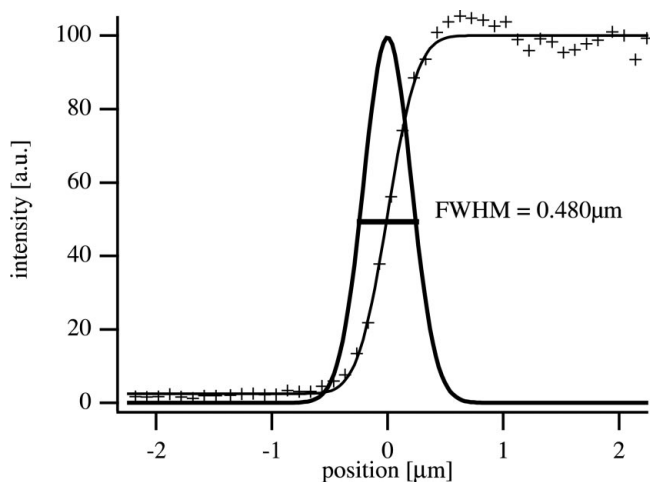

Figure 3
Advantages of parabolic lens profiles as compared with spherical ones. (a) A parabolic embossing tool generates everywhere normal forces which results in a smoother surface. (b) For a parabolic profile the geometric aperture $2R_0$ and the radius of curvature, which determines the focal length, are decoupled.

Fresnel zone plates. Since the optical path is straight, alignment is easy and can be done in 15 minutes.

We have demagnified the source at beamline ID22 of the ESRF with a stack of Al lenses. The radiation was monochromated by means of an Si (111) double-crystal monochromator operating at 18.2 keV. The number of lenses in the stack was $N = 220$ and the radius of curvature was $R = 209 \pm 5\ \mu m$. With a source-to-lens distance of $L_1 = 41.7$ m the optimal image distance was determined experimentally to be $L_2 = 331$ mm, giving a focal distance of 328 mm. This results in a demagnification of the source by a factor of 126. The horizontal and vertical microbeam sizes were measured by a fluorescence technique with a gold knife-edge deposited on silicon. The Au L_α radiation (9.71 keV) was measured by an energy-dispersive SiLi detector. Fig. 4 shows a scan through the microbeam in the vertical direction. A vertical beam width of $B_v = 480$ nm was measured. This compares well with an expected full width at half-maximum (FWHM) size of 450 nm including diffraction and roughness. Note that the low background in the intensity profile is characteristic of high-quality lenses with a low level of small-angle and diffuse scattering. The horizontal spot size of $B_h = 5.17\ \mu m$ (FWHM) is large compared with the vertical spot size B_v, since the horizontal source size is large in the high-β section at beamline ID22 of the ESRF. At a low-β section of the ESRF the undulator source is smaller by a factor of six, resulting in a six times smaller horizontal spot size. The measured gain (intensity in the spot as compared with that behind a pinhole of equal size) was 367.

By using the microbeam produced with the refractive lens, many X-ray analytical techniques, such as diffraction (Castelnau *et al.*, 2001), fluorescence analysis (Bohic *et al.*, 2001; Simionovici *et al.*, 2000; Schroer *et al.*, 2000), absorption spectroscopy and small-angle scattering, can be performed with spatial resolution on the micrometre and submicrometre scale. The small aperture of the lens compared with the image distance L_2 leads to a beam divergence that is sufficiently small for most diffraction experiments ($\Delta k/k < 10^{-3}$).

We now consider imaging by hard X-ray microscopy based on refractive lenses. Just as with a normal microscope, the object is placed slightly outside of the focus of the lens (Lengeler *et al.*, 1999a). Then a strongly magnified picture is generated on a two-dimensional camera. The magnification is given by

$$M = L_2/L_1 = \frac{f}{L_1 - f}. \tag{4}$$

Fig. 5 shows a micrograph ($M = 21$) of a gold test pattern taken with 120 Al lenses ($R = 0.2$ mm) at 25 keV. The period of the test structure is 2 μm, the line width is 1 μm and the thickness is 2 μm.

The lateral resolution for incoherent illumination of the object is given by (Lengeler *et al.*, 1999a)

$$d_t = 0.75\ \frac{\lambda}{2\text{N.A.}} = 0.75\ \frac{\lambda L_1}{D_{\text{eff}}}. \tag{5}$$

The numerical aperture N.A. is given by
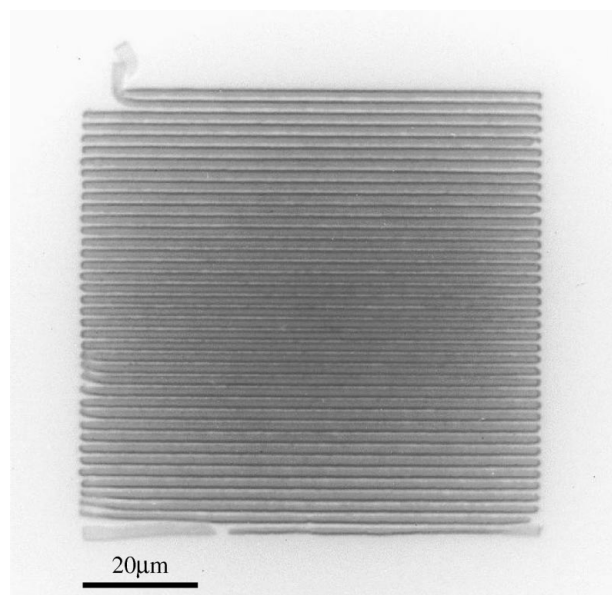
$$\text{N.A.} = \frac{D_{\text{eff}}}{2L_1}$$

where L_1 is the object–lens distance and (Lengeler *et al.*, 1999a)

$$D_{\text{eff}} = 2R_0\left\{\left[1 - \exp(-a_p)\right]/a_p\right\}^{1/2}. \tag{6}$$

D_{eff} is the effective aperture of the lens, reduced by photon absorption and scattering, compared with the geometrical aperture $2R_0$. With aluminium lenses we have reached a resolution of 0.34 μm at 23.5 keV which is close to the theoretical value expected from photoabsorption in Al.

The lower absorption in Be leads to an expected lateral resolution of 80 nm and below. The influence of absorption is also clearly demonstrated in the size of the field of view. Fig. 6 shows two numerically generated images of a Ni mesh (period 50 μm, width of grid wires 10 μm, thickness 10 μm) as imaged at 20 keV in a one-to-one geometry ($f = 2.35$ m, $L_1 = L_2 = 2f$) with a Be and an Al lens (small inset). The parabolic refractive Be lens with 50 lenses in the stack gives a field of view larger than 800 μm. For an Al lens ($N = 31$, all other parameters equal) the field of view is about 200 μm.

Fig. 7 shows the micrograph of a Ni mesh with a 12.5 μm period taken at 25.5 keV with 120 Al lenses and a focal length of 1.05 m. The magnification was $M = 21$. Note the excellent quality of the image very close to the quality expected from the numerical simulation
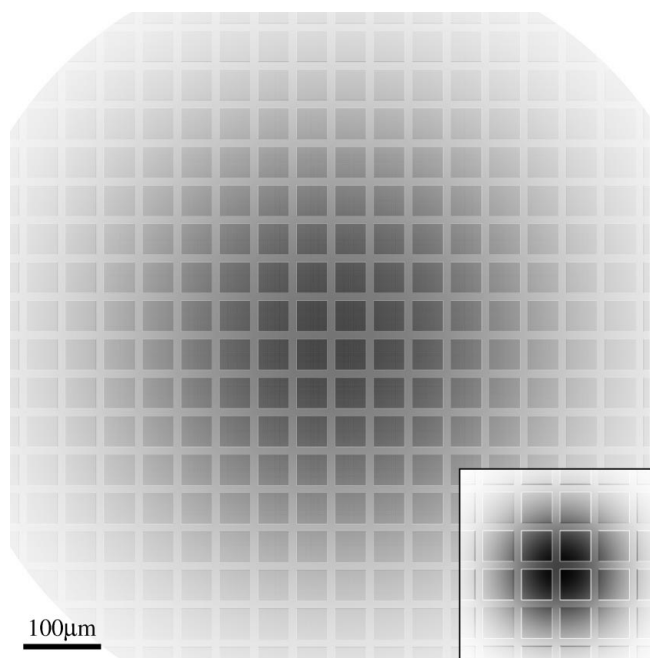

Figure 4
Vertical profile through a microbeam generated by a parabolic refractive X-ray lens at ID22 at the ESRF. An error function is fitted to the data measured by a knife-edge technique. Its derivative gives the vertical width of the spot.

Figure 5
Micrograph of a gold test pattern (period 2 μm, thickness 2 μm) taken at 25 keV with an Al lens ($N = 120$, $R = 0.2$ mm, $f = 1.05$ m). The image of the pattern was magnified ×21 onto a CCD detector ($L_1 = 1.10$ m, $L_2 = 23$ m).

shown in Fig. 8. All numerical simulations are based on Fresnel propagation, where the object is illuminated coherently. The partial coherence of the undulator source is not taken into account. The parabolic shape of the lenses ensures an image free of distortion by spherical aberration. A numerical simulation of the influence of spherical aberration is shown in Fig. 9 for the same nickel mesh. The spherical lenses show a strong cushion-like distortion and other artifacts whereas the parabolic lenses generate a distortion-free image in the simulation (Fig. 8) and in the experiment (Fig. 7).

Today, projection imaging is the most common method in hard X-ray microscopy at storage rings. Its lateral resolution is limited by the detector resolution, which is slightly below 1 µm for the best detectors available today (Koch *et al.*, 1998). This high resolution is obtained at the expense of detector efficiency using thin monocrystalline scintillator films. Since the hard X-ray microscope produces magnified X-ray images, it can alleviate the requirements on the detector resolution while producing images with a higher lateral resolution.
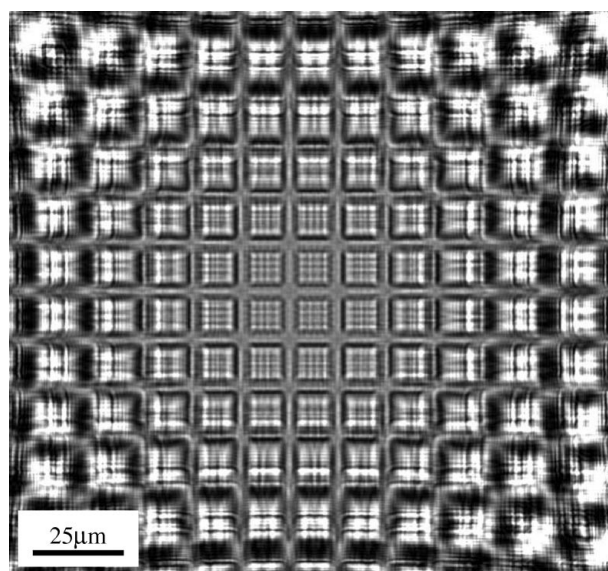

Figure 6
Expected field of view for parabolic refractive beryllium and aluminium X-ray lenses with E = 20 keV, f = 2.35 m, N = 50 for Be and N = 31 for Al. The test pattern is a Ni grid with 50 µm and 10 µm grid width and thickness.
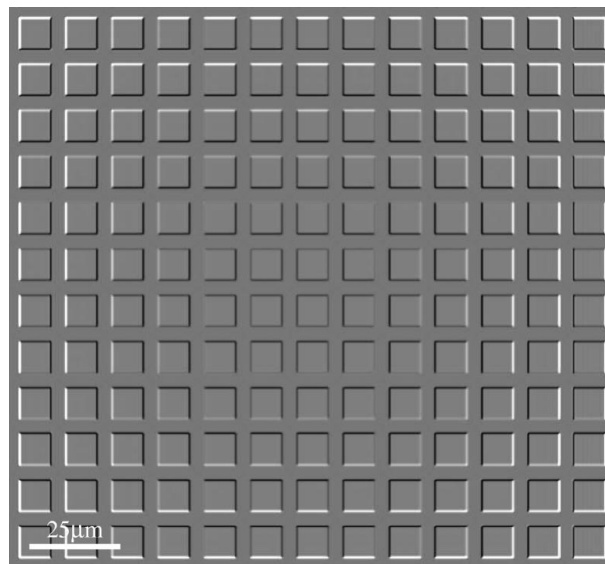
Figure 8
Numerically generated X-ray micrograph of the Ni mesh as imaged in a one-to-one geometry at 25 keV using an aluminium lens with N = 120.
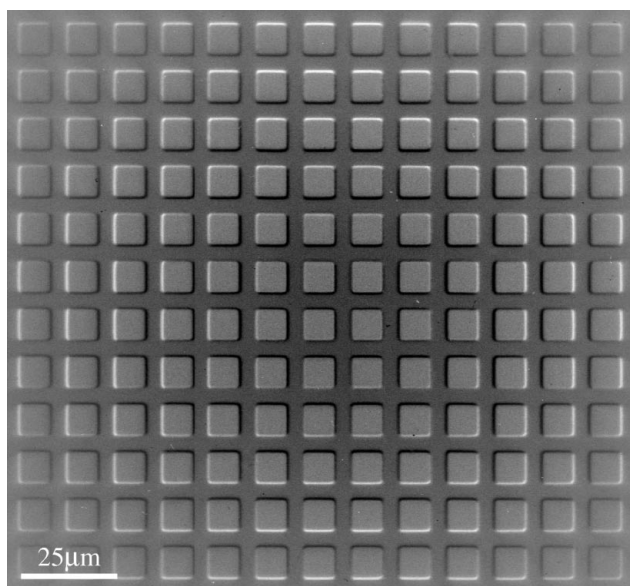
Figure 7
Flat-field-corrected X-ray micrograph of a Ni mesh (2000mesh) recorded with an aluminium lens at 25 keV (N = 120, f = 1.05 m, L_1 = 1.10 m, L_2 = 23 m).
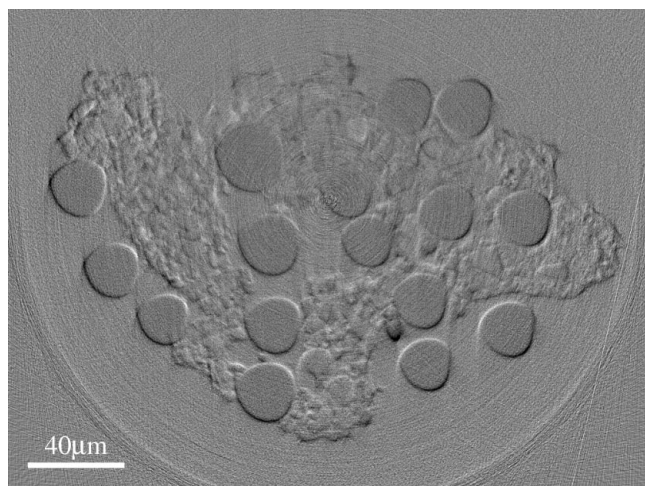

Figure 9
Numerically generated X-ray micrograph of the Ni mesh from Fig. 7 imaged by a stack of spherical Al lenses (N = 120, E = 25 keV). Except for the lens shape, all parameters have been kept the same as for Fig. 8.

One major advantage of hard X-rays is their large penetration depth which allows one to image the interior of a sample. Combining hard X-ray microscopy with tomographic techniques allows the reconstruction of the three-dimensional structure of a sample (Schroer *et al.*, 2001; Rau *et al.*, 2001). For this purpose, a set of X-ray micrographs is recorded as a function of sample rotation at equidistant steps in an angular interval from 0 to 180°. For standard tomographic techniques to be applicable, the X-ray micrographs need to be projection images of the sample that are free of distortion. Owing to the large depth of field, the X-ray micrographs are sharp projections. The parabolic shape guarantees an image free of distortion. For partially coherent illumination of the sample, the contrast in the image plane depends on the position of the sample in the field of view. This contrast and how to cope with it for tomographic imaging is described in detail elsewhere (Schroer *et al.*, 2002). Fig. 10 shows a reconstructed slice through a fibre reinforced concrete sample. 250 X-ray micrographs with ×10.6 magnification were recorded at 20.65 keV using an Al refractive lens ($N = 42$, $f = 1.89$ m). The object distance was $L_1 = 2.07$ m, and the high-resolution CCD detector (FReLoN2000; Weitkamp *et al.*, 1999) was placed at an image distance of $L_2 = 22.03$ m. The slice in Fig. 10 was reconstructed using filtered backprojection. In principle, the three-dimensional resolution in the reconstructed image can be as high as the lateral resolution in single projections. Here, however, the resolution was limited by mechanical instabilities of the rotation and translation stages. The motion of the rotation axis produces, for instance, the distortions of the circular fibres in Fig. 10. The requirements on the rotation stage will become stronger as the lateral resolution in the X-ray images can be improved, for example, by using a more transparent lens materials.

Instead of generating a magnified image of an object we might also be interested in demagnifying the image, as, for example, for lithographical purposes. Up to now, there were no ways to demagnify a mask with hard X-rays. Our lenses can easily demagnify a mask by a factor of ten, thus alleviating substantially the requirements on lithography masks. First tests have been very promising. Another advantage is the large depth of field in X-ray imaging by refractive lenses. Indeed the longitudinal resolution d_l,

$$d_l = 0.64\lambda/(\text{N.A.})^2,$$

Figure 10
Magnified tomographic slice through a fibre reinforced concrete sample. The slice was reconstructed using 250 X-ray micrographs at a magnification of 10.6.

is of the order of millimetres (Lengeler *et al.*, 1999a). This allows one to project a sharp image of a mask into a thick resist and alleviates the requirements on the longitudinal positioning of mask and resist. As opposed to the proximity method, mechanical contact between the delicate mask and the resist can be avoided. However, there are also serious drawbacks. The field of view will at best be 1 mm resulting in the need of stitching in order to expose larger structures. Since refractive lenses show chromatic aberration, quasi-monochromatic radiation must be used for the lithography process. This requires a high spectral brilliance of the X-ray source to avoid long exposure times. Chemically amplified resists, such as SU8, may help to reduce exposure times but introduce other difficulties.

References

Aristov, V., Grigoriev, M., Kuznetsov, S., Shabelnikov, L., Yunkin, V., Weitkamp, T., Rau, C., Snigireva, I. & Snigirev, A. (2000). *Appl. Phys. Lett.* **77**, 4058–4060.

Aristov, V. V., Basov, Y. A., Kulipanov, G. N., Pindyurin, V. F., Snigirev, A. A. & Sokolov, A. S. (1989). *Nucl. Instrum. Methods A*, **274**, 390.

Bilderback, D., Hoffman, S. A. & Thiel, D. (1994). *Science*, **263**, 201–203.

Bohic, S., Simionovici, A., Snigirev, A., Ortega, R., Devès, G., Heymann, D. & Schroer, C. G. (2001). *Appl. Phys. Lett.* **78**, 3544–3546.

Castelnau, O., Drakopoulos, M., Schroer, C. G., Tümmler, J. & Lengeler, B. (2001). *Nucl. Instrum. Methods A*, **467/468**, 1245–1248.

Cederström, B., Cahn, R. N., Danielsson, M., Lundqvist, M. & Nygren, D. R. (2000). *Nature (London)*, **404**, 951.

Cederström, B., Danielsson, M. & Lundqvist, M. (2001). In *Advances in X-ray Optics*, edited by A. K. Freund, T. Ishikawa, A. M. Khounsary, D. C. Mancini, A. G. Michette & S. Oestreich, Vol. 4145 of *Proceedings of the SPIE*, pp. 294–302.

Chevallier, P., Dhez, P., Legrand, F., Idir, M., Soullie, G., Mirone, A., Erko, A., Snigirev, A., Snigereva, I., Suvorov, A., Freund, A., Engström, P., Nielsen, J. A. & Grübel, A. (1995). *Nucl. Instrum. Methods A*, **354**, 584–587.

Dudchik, Y. I., Kolchevsky, N. N., Komarov, F. F., Kohmura, Y., Awaji, M., Suzuki, Y. & Ishikawa, T. (2000). *Nucl. Instrum. Methods A*, **454**, 512–519.

Elleaume, P. (1998). *Nucl. Instrum. Methods A*, **412**, 483–506.

Feng, Y. P., Sinha, S. K., Deckman, H. W., Hastings, J. B. & Siddons, D. S. (1998). *Phys. Rev. Lett.* **71**, 537–540.

Hignette, O., Rostaing, G., Cloetens, P., Rommeveaux, A., Ludwig, W. & Freund, A. (2001). In *X-ray Micro- and Nano-Focusing: Applications and Techniques II*, edited by I. McNulty, Vol. 4499 of *Proceedings of the SPIE*, pp. 105–116.

Hoffman, S. A., Thiel, D. J. & Bilderback, D. H. (1994). *Nucl. Instrum. Methods A*, **347**, 384.

Kirkpatrick, P. & Baez, A. (1948). *J. Opt. Soc. Am.* **38**, 766–774.

Koch, A., Raven, C., Spanne, P. & Snigirev, A. (1998). *J. Opt. Soc. Am. A*, **15**, 1940–1951.

Kohmura, Y., Awaji, M., Suzuki, Y., Ishikawa, T., Dudchik, Y. I., Kolchewsky, N. N. & Komarow, F. F. (1999). *Rev. Sci. Instrum.* **70**, 4161–4167.

Lagomarsino, S., Cedola, A., Cloetens, P., Di Fonzo, S., Jark, W., Soullié, G. & Riekel, C. (1997). *Appl. Phys. Lett.* **71**, 2557–2559.

Lai, B., Yun, W., Legnini, D., Xiao, Y., Chrzas, J., Viccaro, P., White, V., Bajikar, S., Denton, D., Cerrina, F., Fabrizio, E., Gentili, M., Grella, L. & Baciocchi, M. (1992). *Appl. Phys. Lett.* **61**, 1877–1879.

Lengeler, B., Schroer, C., Tümmler, J., Benner, B., Richwin, M., Snigirev, A., Snigireva, I. & Drakopoulos, M. (1999a). *J. Synchrotron Rad.* **6**, 1153–1167.

Lengeler, B., Schroer, C. G., Richwin, M., Tümmler, J., Drakopoulos, M., Snigirev, A. & Snigireva, I. (1999b). *Appl. Phys. Lett.* **74**, 3924–3926.

Piestrup, M. A., Cremer, J. T., Beguiristain, H. R., Gary, C. K. & Pantell, R. H. (2000). *Rev. Sci. Instrum.* **71**, 4375–4379.

Rau, C., Weitkamp, T., Snigirev, A., Schroer, C. G., Tümmler, J. & Lengeler, B. (2001). *Nucl. Instrum. Methods A*, **467/468**, 929–931.

Schroer, C. G., Benner, B., Günzler, T. F., Kuhlmann, M., Lengeler, B., Rau, C., Weitkamp, T., Snigirev, A. & Snigireva, I. (2002). In *Developments in X-ray Tomography III*, edited by U. Bonse, Vol. 4503 of *Proceedings of the SPIE*, pp. 23–33.

Schroer, C. G., Günzler, T. F., Benner, B., Kuhlmann, M., Tümmler, J., Lengeler, B., Rau, C., Weitkamp, T., Snigirev, A. & Snigireva, I. (2001). *Nucl. Instrum. Methods A*, **467/468**, 966–969.

Schroer, C. G., Tümmler, J., Günzler, T. F., Lengeler, B., Schröder, W. H., Kuhn, A. J., Simionovici, A. S., Snigirev, A. & Snigireva, I. (2000). In *Penetrating Radiation Systems and Applications II*, edited by F. P. Doty, H. B. Barber, H. Roehrig & E. J. Morton, Vol. 4142 of *Proceedings of the SPIE*, pp. 287–296.

Simionovici, A. S., Chukalina, M., Schroer, C., Drakopoulos, M., Snigirev, A., Snigireva, I., Lengeler, B., Janssens, K. & Adams, F. (2000). *IEEE Trans. Nucl. Sci.* **47**, 2736–2740.

Snigirev, A., Kohn, V., Snigireva, I. & Lengeler, B. (1996). *Nature (London)*, **384**, 49.

Underwood, J., Barbee, T. Jr & Frieber, C. (1986). *Appl. Opt.* **25**, 1730–1732.

Underwood, J., Thompson, A., Wu, Y. & Giauque, R. (1988). *Nucl. Instrum. Methods A*, **266**, 296–302.

Weitkamp, T., Raven, C. & Snigirev, A. (1999). In *Developments in X-ray Tomography II*, edited by U. Bonse, Vol. 3772 of *Proceedings of the SPIE*, pp. 311–317.